

# Mapping critical density surface of plasma mirrors from wavefront measurements

PPr1001 Project Report

Submitted to  
**UM-DAE Centre for Excellence in Basic Sciences**  
**Mumbai - 400098, India**

in partial fulfilment of the requirements  
for the award of the degree of

**Integrated M.Sc. (Physics)**



by

**Varun Joshi**

(Roll No. P0201452)

Under the Supervision of

**Prof. G Ravindra Kumar**

Department of Nuclear and Atomic Physics  
TIFR, Mumbai

May, 2025

# Certificate

This is to certify that **Varun Joshi** (Roll No.: P0201452) has undertaken his project under the guidance of **Prof. G Ravindra Kumar** at TIFR, Mumbai.

This report titled “**Mapping critical density surface of plasma mirrors from wavefront measurements**” is submitted to UM-DAE CEBS, Mumbai towards the institute’s academic requirements for the 10<sup>th</sup> semester (PPr1001) of the Int. M.Sc. degree (Physics).

**Student Name & Signature**



.....  
**Varun Joshi**

Roll No.: P0201452

**Guide Name & Signature**



...  
**Prof. G Ravindra Kumar**

Department of Nuclear and Atomic Physics  
TIFR, Mumbai.

Date: 2<sup>nd</sup> May 2025

# *Acknowledgements*

I take this opportunity to acknowledge and express my gratitude to all those who supported and guided me in the duration of this project.

The biggest thanks goes to Prof. G Ravindra Kumar (Ravi). He is an exemplary teacher and physicist, and a figure of inspiration. I attended his classes in the previous year and was hooked to his interactive way of teaching, so I decided to write to him to work in his lab. He always emphasizes on looking at problems in the simplest way possible. I can honestly say that I have learnt more in our discussions than hours of reading a book or article.

I am fortunate to have interacted with very supportive and welcoming seniors and colleagues at UPHILL lab. I thank Rakeeb, Sagar and Ameya for their personal and academic help throughout the project. Looking at how they help each other in numerous ways- from setting up experiments to heated discussions and constructive criticism, I have learnt how members in a research group can actively collaborate and support each other.

I also thank my friends Abhay and Adityamani for constantly being in touch and supporting me. At last, I would like to thank my family for their unwavering support and affection.

Varun Joshi

# *Abstract*

Collective behaviour of charged particles in a plasma allows us to view it as an optical medium of properties that can be tailored by playing with density, temperature and mass of the constituent particles. Interaction of plasmas with electromagnetic waves provides a means to understand these properties. High intensities achieved by focusing light from a coherent source, such as a pulsed *laser* on matter can ionize it to create this plasma in the first place. To capture the subsequent dynamics, a replica of the ionizing 'pump' pulse is used to interrogate (probe) the plasma at different time delays by measuring the changes incurred in it.

In the duration of this project, we use an achromatic wavefront measurement technique to capture the shape of the surface of plasma generated by a high-contrast intense femtosecond laser pulse falling on a solid target. We address this in two different ways. First is the evolution of the shape of this surface in time, that is achieved by performing a time-varying measurement using the Pump-Probe technique. In the second, we find how the curvature in the plasma surface scales with the laser intensity. Instead of a regular pump-probe measurement, the reflected pump is measured so that a cumulative effect of changes happening only within the duration of the pulse are captured.

Wavefront measurements of the reflected pump show what could potentially be a first account of optical signatures of the laser ponderomotive force. The ponderomotive force is a non-linear force that exists due to gradients in electric field. It is an important phenomenon in laser-plasma interaction and plays a role in laser absorption processes and plasma instabilities.

# Contents

Certificate

Acknowledgements

Abstract

Contents

<b>1</b>	<b>Intense Laser-Matter Interactions: An Introduction</b>	<b>1</b>
1.1	Atoms in Extreme Light . . . . .	2
1.2	Extreme light on solids . . . . .	3
1.3	Ponderomotive force of an optical field . . . . .	4
1.4	Laser propagation and absorption mechanisms . . . . .	5
<b>2</b>	<b>Experimental Methods</b>	<b>8</b>
2.1	TIFR Terawatt Laser System . . . . .	8
2.1.1	Spectrum . . . . .	10
2.1.2	Pulse characterization . . . . .	10
2.2	The Pump-Probe Experimental Setup . . . . .	11
<b>3</b>	<b>Wavefront measurement of laser-generated plasma</b>	<b>14</b>
3.1	Lateral Shearing Interferometry . . . . .	14
3.2	The Hartmann Mask as a lateral shearing interferometer . . . . .	15
3.3	The Modified Hartmann Mask (MHM) . . . . .	18
3.4	The experiments . . . . .	20
3.4.1	Time evolution of the critical density surface . . . . .	20
3.4.2	Scaling of surface modulation with intensity . . . . .	21
<b>4</b>	<b>Results and Conclusions</b>	<b>22</b>
4.1	Time evolution of critical density surface . . . . .	22
4.2	Critical surface curvature at different intensities . . . . .	23
4.3	Future prospects for wavefront measurement . . . . .	24



# Chapter 1

## Intense Laser-Matter Interactions: An Introduction

Lasers are devices that produce or amplify electromagnetic radiation in the optical region [[Siegman \(1986\)](#)]. Their coherence, intensity and directionality make them a distinctive source of light. Since their development, lasers have found a wide range of applications in areas ranging from physics, bio-imaging, semiconductor industry to guided weaponry. Short-pulse lasers represent a special class of lasers that are designed to emit intense flashes of light for extremely short durations. A major outcome of compressing energy into short-duration pulses is the ability to reach extremely high intensities. Advances in the development of more and more powerful pulsed lasers, such as the method of Chirped Pulse Amplification (CPA)[[Strickland and Mourou \(1985\)](#)], allow us to routinely reach laser electric fields that exceed, by orders of magnitude, the Coulomb field of nuclei on their electrons!

Evidently, any material that comes in way of such high electric fields gets instantly ionized, making it a plasma. The laser pulse not only produces this plasma, but can also be used to capture its dynamics. By recording modifications on a well-described laser pulse, ultrafast dynamics of various fundamental plasma processes can be probed with the laser. From the creation of this plasma, to the mechanisms of energy coupling from the laser field to the plasma, this chapter is a chronological description of events that occur when an ultrashort intense laser falls on matter.

## 1.1 Atoms in Extreme Light

Under extremely high electric fields of a pulsed laser, electrons in the ground state can be lost to ionization. Depending upon how this field compares to the Coulomb field of the nucleus on the electrons, various mechanisms of ionization can be described (See Fig. 1.1). We also learn which mechanism plays more role depending upon the laser parameters.

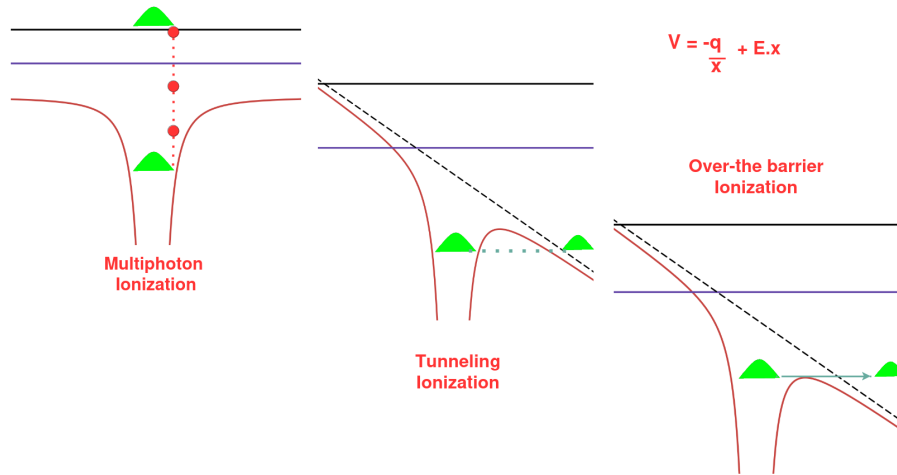


FIGURE 1.1: Mechanisms of ionization in a laser field

Contrary to absorption/emission at moderate intensities, **multiphoton ionization** is a process in which an atom or a molecule absorbs 2 or more photons simultaneously to move from a lower energy to a higher energy state (or become unbound). The rate of ionization ( $\Gamma_n$ ) associated with an  $n$  photon absorption process is proportional to the light intensity raised to the power  $n$ ,

$$\Gamma_n = \sigma_n I_L^n \quad (1.1)$$

This relation, however, breaks down when the laser electric field is comparable or larger than the Coulomb field of the atom. At light intensities  $\sim 10^{16}$  W/cm<sup>2</sup> the laser electric field reaches close to the atomic field and severely distorts the electric potential allowing for **tunnelling ionization** of the electron. The distortion happens with every half cycle of the optical pulse, so the electron should tunnel faster than the oscillation of the electric field. Keldysh developed the theory of tunneling ionization by taking the Coulomb potential as a perturbation to the laser potential.



To decide the propensity of this ionization mechanism, he defined a parameter,  $\Gamma$ , which is the ratio of the laser frequency to the tunneling frequency :

$$\Gamma = \frac{\omega}{\omega_{tunnel}} \quad (1.2)$$

This mechanism is dominant only when the parameter  $\Gamma < 1$ . For  $\Gamma > 1$ , Multi-photon ionization is dominant. At even higher intensities, the electron is no longer bound by the Coulomb potential and can freely escape. This mechanism is called **over-the-barrier ionization**. The threshold can be calculated by equating the distortion of the laser electric field to that of the Coulomb field.

## 1.2 Extreme light on solids

When the laser falls on a solid with a density of the order of  $10^{23} / \text{cm}^3$ , the ionization processes create a hot-dense plasma. The temporal profile of the pulsed laser, in reality, has a pedestal which is of the order of picoseconds or longer with a femtosecond peak. The picosecond pedestal can be attributed to any residual amplification of spontaneous emission (ASE) in the lasing medium. So, the femtosecond peak is preceded by a weaker pulse, which is sufficient to form a *pre-plasma* before the femtosecond pulse arrives (see Fig. 1.2). In the remaining part of the report, we will describe the interaction in terms of a femtosecond pulse interacting with an inhomogeneous plasma that has a density scale length.

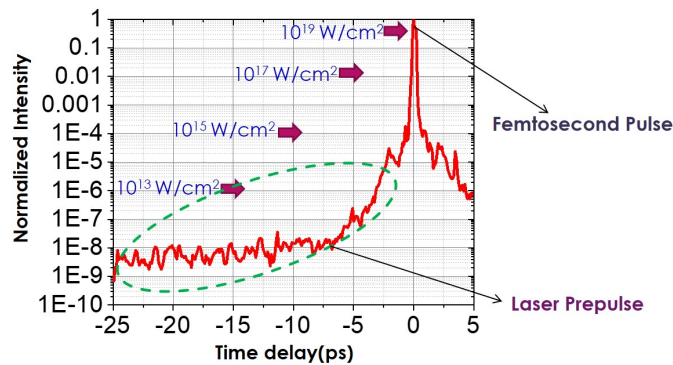


FIGURE 1.2: Contrast of the laser pulse. Courtesy: Sagar Dam

### 1.3 Ponderomotive force of an optical field

[Eliezer (2002)]

In reality, any optical field has space-variation and can be described as

$$E(r, t) = E_s(r) \cos \omega t \quad ; \quad B(r, t) = B_s(r) \sin \omega t = -\frac{c}{\omega} \nabla \times E_s(r) \sin \omega t \quad (1.3)$$

An electron in such a field experiences a force which can be written as the following in Gaussian units:

$$m \frac{d\mathbf{v}}{dt} = -e(\mathbf{E}_s \cos \omega t + \frac{v}{c} \times \mathbf{B}_s \sin \omega t) \quad (1.4)$$

For sufficiently low intensities, the magnetic component can be neglected ( $v \ll c$ ) and the force equation becomes:

$$m \frac{dv}{dt} = qE_s \quad \Rightarrow \quad v_1 = \frac{eE_s(r_0)}{m\omega} \sin \omega t \quad \Rightarrow \quad v_{max} = \frac{eE_s(r_0)}{m\omega} \quad (1.5)$$

We define a dimensionless parameter  $a_0$

$$a_0 = \frac{v_{max}}{c} = \frac{p}{m_e c} = \frac{eE_s}{m\omega c} \approx 0.855 \sqrt{I_{18} \lambda_\mu^2} \quad (1.6)$$

Where  $I_{18}$  is the intensity in multiples of  $10^{18} \text{ W/cm}^2$  and  $\lambda_\mu$  is the wavelength in microns.  $a_0 > 1$  corresponds to high intensity and relativistic electrons, in which case (1.4) has to be modified.

For non-relativistic intensities described in (1.5), we have

$$r_1 = \frac{eE_s}{m\omega^2} \cos \omega t \quad (1.7)$$

This is assuming there is no effect of space variation in  $E_s$ . When this variation is taken into account, we have

$$E_s = E_S(r_0) + (r_1 \cdot \nabla) E_s|_{r=r_0} \quad ; \quad v = v_1 + v_2 \quad (1.8)$$

and the equation of motion for the second term in  $v$  is

$$m_e \frac{dv_2}{dt} = -e \left[ (r_1 \cdot \nabla) E_s(r_0) \cos \omega t + \frac{v_1 \times B_s(r_0) \sin \omega t}{c} \right] \quad (1.9)$$

Using 1.5, substituting  $B$  from 1.3 and averaging over one optical cycle ( $\langle \sin^2 \omega t \rangle = \langle \cos^2 \omega t \rangle = 1/2$ ), we get the expression for non-linear force acting on the electron

$$F_{nl} = m_e \left\langle \frac{dv_2}{dt} \right\rangle = \frac{-e^2}{2m_e \omega^2} [(E_s \cdot \nabla) E_s + E_s \times (\nabla \times E_s)] \quad (1.10)$$

using the identity

$$E_s \times (\nabla \times E_s) = (\nabla E_s) \cdot E_s - (E_s \cdot \nabla E_s) E_s = \frac{1}{2} \nabla \cdot E_s^2 - (E_s \cdot \nabla) E_s$$

the expression for  $F_{nl}$  reduces to

$$F_{nl} = \frac{-e^2}{4m_e \omega^2} \nabla E_s^2 \quad (1.11)$$

It is a time averaged non-linear force that exists when there is a spatial gradient in electric field. It acts in the direction opposite to the gradient and is independent of charge sign( $\pm$ ). Electrons and ions move in the same direction in its presence and it is called the **ponderomotive force** (*ponderous*: heavy, *motive*: moving) as it moves the bulk of charges, positive and negative. Relativistic corrections in the derivation of ponderomotive force for high intensities can be found in [Mulser and Bauer \(2010\)](#).

In a plasma with charge density  $n_e$ , the ponderomotive force per unit volume is written as

$$f_p = n_e F_{nl} = \frac{-n_e e^2}{4m_e \omega^2} \nabla E_s^2 = \frac{-\omega_{pe}^2}{16\pi \omega^2} \nabla E_s^2 \quad (1.12)$$

where  $\omega_{pe}$  is the electron plasma frequency described in the next section.

## 1.4 Laser propagation and absorption mechanisms

[\[Kruer \(2003\)\]](#)

Plasma with its ability to support waves or collective modes can sustain charge density fluctuations at a characteristic frequency determined by the electrons and/or the ions. There are two such plasma waves: an electron plasma wave of high frequency and an ion acoustic wave of low frequency.

The electron plasma frequency, denoted as  $\omega_{pe}$ , describes the natural oscillation frequency of electrons in a plasma when displaced from their equilibrium position. Consider an electron plasma with number density  $n_0$  and electrons of mass  $m_e$  and charge  $-e$ . The restoring force on an electron due to a displacement  $x$  in a uniform plasma is:

$$F = -eE,$$

where  $E$  is the electric field caused by the charge distribution. Using Gauss's law for a uniform charge distribution in Gaussian units, the electric field becomes:

$$E = 4\pi n_0 ex \quad \Rightarrow \quad m_e \frac{d^2x}{dt^2} = -4\pi n_0 ex.$$

Which resembles a simple harmonic oscillator equation, with angular frequency  $\omega_{pe}$ :

$$\omega_{pe} = \sqrt{\frac{4\pi e^2 n_0}{m_e}} \quad (1.13)$$

When light waves of frequency  $\omega$  propagate through the plasma, the dispersion relation is given as

$$\omega^2 = \omega_{pe}^2 + k^2 c^2 \quad (1.14)$$

The condition  $\omega = \omega_{pe}$  defines a critical plasma density over which the radiation of frequency  $\omega$  cannot penetrate the plasma. It is expressed as  $n_c = 1.1 \times 10^{21} / \lambda_\mu^2 \text{ cm}^{-3}$  where  $\lambda_\mu$  is the laser wavelength expressed in microns.

As the pedestal laser couples its energy to the plasma, the plasma grows and develops a longitudinal density gradient. The implication is that light of a certain wavelength can only propagate up to a certain skin depth associated with the corresponding critical density. This longitudinal density gradient gives rise to the most dominant absorption mechanism, known as **resonance absorption**.

When a p-polarized laser pulse is incident at an angle on the pre-plasma, it propagates up to density  $n_e = n_c \cos^2 \theta$  and some of it reflects (see Fig. 1.3). Critical density corresponds to the surface where the laser frequency is resonant with the electron motion in the plasma wave. This resonance enhances the charge density fluctuations at the critical surface and the laser energy couples to the electrons at this surface, which is then diffused into the plasma by collisions and other mechanisms.

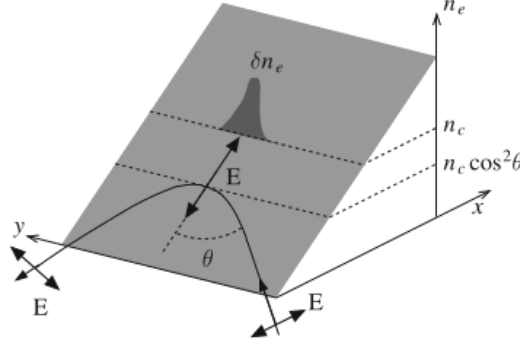


FIGURE 1.3: Resonance absorption of a p-polarized pulse obliquely incident on an inhomogeneous plasma. Taken from [Macchi \(2013\)](#)

When a moving charge gets accelerated due to the presence of other particles and fields, it radiates braking radiation (bremsstrahlung). The inverse of this process happens when a charged particle like electron absorbs light. This process is called "inverse bremsstrahlung" or **collisional absorption**. The absorption fraction of this mechanism increases with the collision frequency ( $\nu_{ie}$ ) and plasma scale length ( $L$ ). Since  $\nu_{ie}$  scales as  $T^{-3/2}$ , this mechanism is not dominant for high intensities ( $> 10^{15} \text{ W/cm}^2$ ) which correspond to high electron temperatures.

Both the mechanisms defined above depend upon pre-plasma scale length and do not play a significant role when the laser pulse is extremely clean, so that the scale length is very short ( $L \ll \lambda$ ) at the arrival of the femtosecond peak. For high intensities, the  $v \times B$  term in the force equation cannot be neglected and leads to another laser absorption mechanism known as  **$\mathbf{J} \times \mathbf{B}$  heating** [[Kruer and Estabrook \(1985\)](#)].

A linearly polarised light  $E = E_0 \hat{y} \sin \omega t$  leads to a longitudinal force

$$f_x = -\frac{m}{4} \frac{\partial v_{osc}^2}{\partial x} (1 - \cos 2\omega t)$$

where the 1st term represents DC ponderomotive force and the second term oscillates with twice the driving laser frequency. This force becomes dominant for relativistic intensities when the quiver velocity, and hence the  $v \times B$  term becomes large.

# Chapter 2

## Experimental Methods

This project deals with the research work aimed at understanding the interaction of an ultrashort ultra-intense laser with solid targets. This chapter is a description of methods and equipment used for the research. The first part describes the TIFR 150 TW laser system along with its pulse characterization methods, followed by a discussion of the experimental techniques used to get results for the experiment. Wavefront measurement of ultrafast laser-generated relativistic plasma is described in the subsequent chapters.

### 2.1 TIFR Terawatt Laser System

The experiments and results discussed in this thesis were performed at the **Ultrashort Pulse High Intensity Laser Laboratory (UPHILL)** at TIFR Mumbai which houses a 150 TW ( $150 \times 10^{12}$  W) Titanium-doped Sapphire (Ti:Sa) laser with a pulse duration  $\sim 25$  fs and per-pulse energy  $\sim 3.5$  J. The laser uses the **Chirped-Pulse Amplification (CPA)** technique [Strickland and Mourou (1985)] to amplify the energy of a femtosecond seed pulse fed by an **oscillator**. The oscillator is an ultrashort laser in itself. It uses a diode laser to pump a Sapphire crystal heavily doped with Titanium. The crystal has a gain bandwidth, allowing for amplification of a range of frequencies. Out of these, only the modes allowed by the length of the laser cavity are sustained, dictated by boundary conditions. Addition of these allowed modes in

phase, achieved by a process called **mode-locking**, causes them to constructively add in a very short temporal span (see Fig. 2.1), giving an ultrashort pulse. The lower limit of pulse duration is decided by the gain bandwidth of the crystal. Higher gain bandwidth is required for shorter pulses.

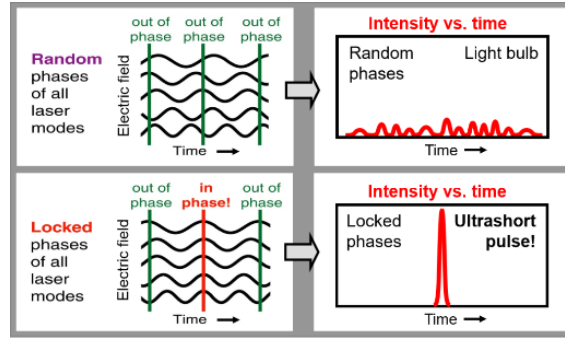


FIGURE 2.1: Mode-locking to produce ultrashort pulses. Courtesy: [Rick Trebino](#)

Direct amplification of a femtosecond pulse would lead to damage of the amplifier optics. To amplify it, therefore, it is stretched in time with the help of a pair of gratings that use angular dispersion of the pulse spectrum to create a differential path length and hence relative time delay, called Group Delay Dispersion, for the range of frequencies in the pulse spectrum. The femtosecond pulse gets stretched up to nanoseconds. This nanosecond pulse is amplified from  $\sim \text{nJ}$  through a series of amplification stages to  $\sim \text{J}$ . Temporal stretching of the amplified pulse can be undone by a similar pair of gratings called the compressor, positioned to compensate for the differential path difference created by the stretcher. A schematic of this technique is explained in Fig 2.2.

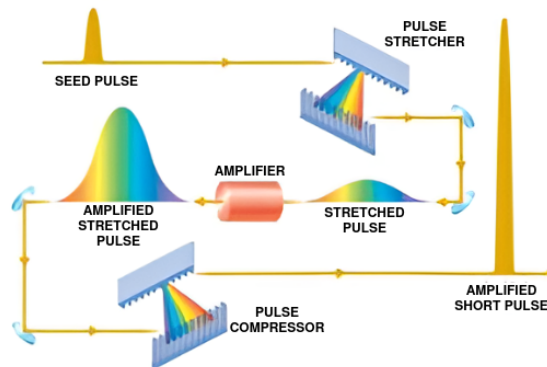


FIGURE 2.2: A schematic of the CPA technique. Taken from [Asplund et al. \(2019\)](#)

### 2.1.1 Spectrum

The spectrum of the 800 nm laser pulse is shown in Fig 2.3. The spectral bandwidth (FWHM) is  $\approx 50$  nm and according to the Fourier transform limit (2.1)[Weiner (2009)] for a Gaussian pulse, it can be compressed down to 25-30 fs.

$$\Delta\nu\Delta t \geq 0.44 \quad (2.1)$$

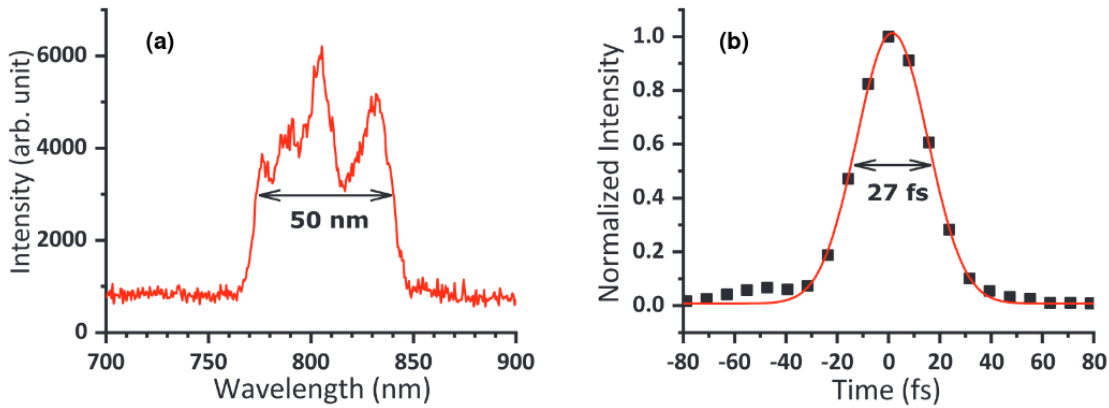


FIGURE 2.3: (a) Spectrum of the 800 nm laser; (b) Pulsewidth measured using SPIDER. Taken from Aparajit et al. (2021)

### 2.1.2 Pulse characterization

The laser system uses Spectral Phase Interferometry for Direct Electric Field Reconstruction (SPIDER) [Iaconis and Walmsley (1998)]. In order to measure an ultrashort pulse, SPIDER splits it into two, then shifts the spectrum of one of the replicas by a known amount. The pulses are sheared across frequency and overlapped in a non-linear medium. The output of this is analysed by a phase retrieval algorithm to obtain the temporal profile of the electric field variation within pulse.



## 2.2 The Pump-Probe Experimental Setup

To capture a process evolving in time, we need another reference event which is at least as brief as the event to be measured. Electronic devices, that respond in the nanosecond timescale, cannot be used to record events shorter than that. An optical measurement has the best shot at achieving such a resolution.

The Pump-Probe method is one such technique (see Fig 2.4). The concept is as follows: A short, intense laser pulse (the "pump") excites a system, initiating a dynamic process, which is the evolution of a plasma in our experiment. A second, weaker pulse (the "probe") arrives after a controlled time delay to interrogate the system. The measurements are made by recording changes in the probe pulse, such as reflectivity, Doppler shift, polarization and phase changes. Assuming that a phenomenon occurring during the process is changing properties of the probe, its associated quantity can be back-calculated by measuring the reflected probe. The resolution in time is dictated by the duration of the pulse and how precise the delay can be controlled. By varying the time delay between the pump and probe pulses with high precision, a time-resolved "snapshot" of the system's evolution can be recorded, mapping its dynamics on ultrafast timescales.

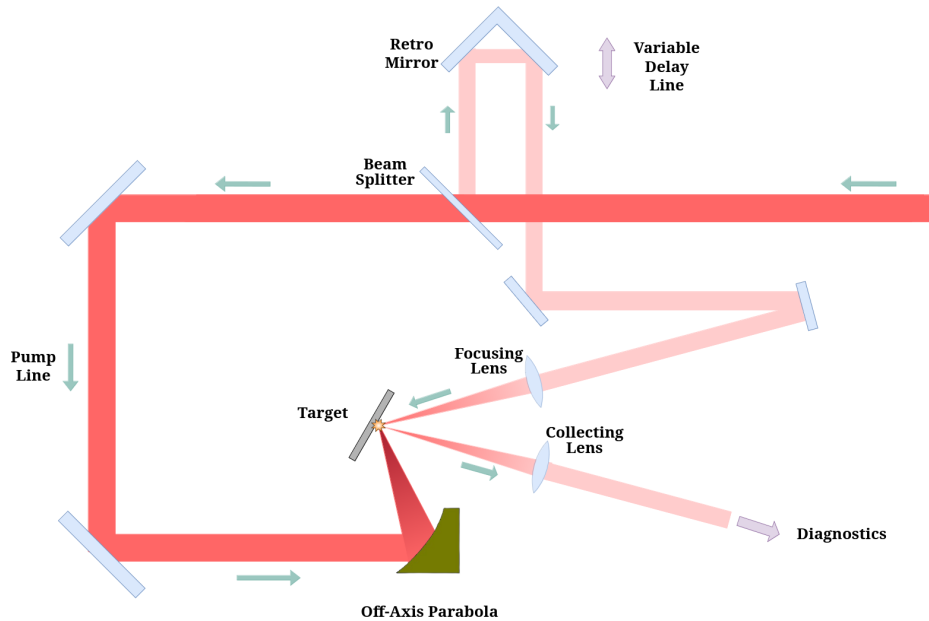


FIGURE 2.4: A schematic of the experimental setup demonstrating the pump-probe technique

After amplification and compression, the beam is routed to the experimental chamber by a series of bending mirrors. In the compressor, the beam line and the experiment chamber, a vacuum of  $\sim 10^{-5}$  mbar is maintained to avoid pulse stretching and any background ionization. For the same reason, a parabolic mirror is used to focus the laser beam onto the target. The incident 8 cm wide beam is focused to a spot of  $\approx 7\mu\text{m}$  (see Fig. 2.5). High pulse power confined to a small target area leads to extreme light intensities of the order of  $10^{18-19}$  W/cm<sup>2</sup> required for the experiment.

After entry into the chamber, a fraction ( $\sim 5\%$  energy) of the beam is leaked to be used as a *probe* for measuring properties of the plasma (Fig. 2.4). For this the probe is focused to the same location as the pump and can be given a variable delay on the target with respect to the pump by passing it through a movable retro mirror.

## Focal Spot Size Imaging

A digital camera is mounted inside the vacuum chamber on the same stage as the target. With a lens of known magnification, it is used to precisely measure the laser focal spot size at low intensities (see Fig. 2.5). It is crucial to measure the spot size as it dictates the light intensity and its effects on the mechanisms of plasma formation and subsequent laser absorption. A precision motorized mount is used to fine tune the x, y orientation and rotation of the parabola to optimize the laser focal spot using feedback from the camera screen.

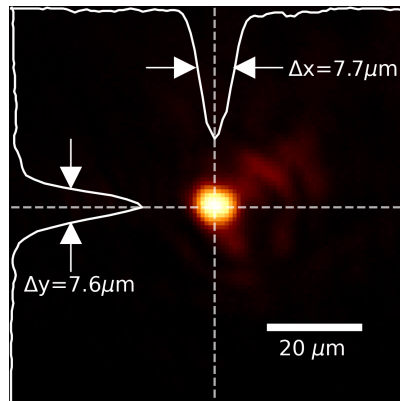


FIGURE 2.5: Imaging of focal spot on a digital camera

## $T_0$ matching by reflectivity measurement

To control the optical delay, we mount a retro mirror on a linear stage. Moving the stage by a distance  $\ell$  corresponds to a delay of  $2\ell/c$ . To give an estimate, a movement of 1 mm would correspond to a time shift of  $\approx 6.7$  ps.

We must know which position of the retro mirror corresponds to zero time delay, i.e. the 'instant' at which the pump and probe overlap in time. To do this we need to employ some property of the plasma which changes dynamically and can be used as a marker of reference time. As an example, let the laser fall on a glass target. We know that the reflectivity of glass is roughly 4%, but after ionization, owing to a surge of free electrons, the plasma becomes metallic in nature. Reflectivity shoots up sharply as the plasma is created, and then decays as the free electron density reduces because of plasma absorption, plasma expansion and electron-ion recombination. We use the pump-probe method to measure the reflectivity as a function of delay and assign our  $T_0$  (or time zero) position to be the one corresponding to the peak in reflectivity (see fig 2.6). Time delays are then assigned with respect to this zero position.

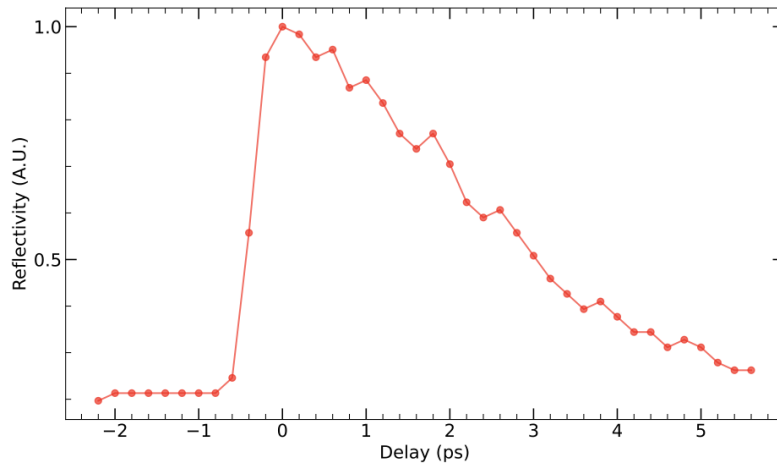


FIGURE 2.6: Reflectivity of glass target as a function of probe delay.  $T_0$  has been taken corresponding to the peak in reflectivity.

## Chapter 3

# Wavefront measurement of laser-generated plasma

Any measurement is an act of comparison against a reference. Often enough, we may not have such a reference and we employ a very radical approach, which is to measure a signal against itself. An example is the measurement of ultrashort pulses where a shorter reference timescale is not readily available and pulses are characterized by obtaining signals of a replicate pulse smearing across the original pulse [\[2.1.2\]](#). A similar approach is taken to measure wavefronts using lateral shearing interferometry.

### 3.1 Lateral Shearing Interferometry

We describe an arbitrary wavefront in terms of its deviation from a flat plane, expressed as wavefront error function  $W(x, y)$  whose value varies laterally across the surface. We take a replica of this wavefront and laterally shear it with some distance  $S$ . Constructive interference happens between the two for loci described by

$$\Delta W(x, y) = n\lambda$$

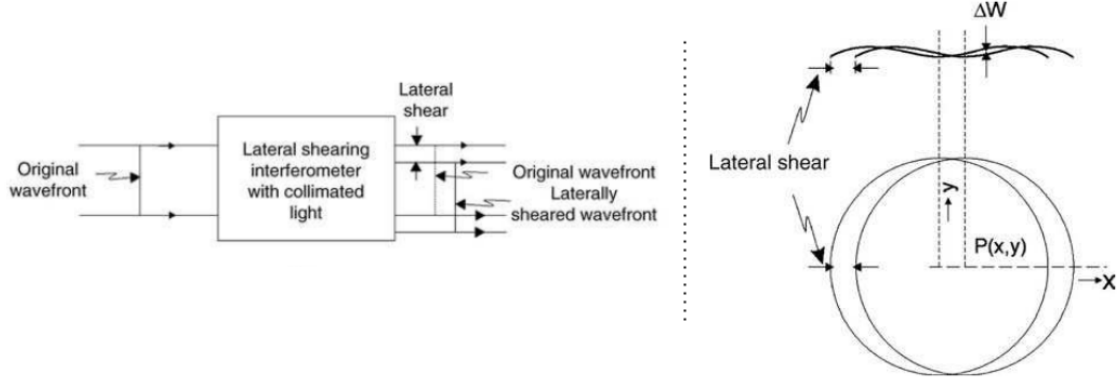


FIGURE 3.1: Lateral Shearing Interferometry. Wavefront is reconstructed by measuring changes in wavefront error ( $\Delta W$ ) with lateral shear. Taken from [Strojnik et al. \(2007\)](#)

Suppose the replica is sheared by an arbitrarily small distance, then we can rewrite the equation as:

$$\frac{\partial W(x, y)}{\partial x} S = n\lambda \quad (3.1)$$

$\frac{\partial W}{\partial x}$ , found by interferometry, can give information of the wavefront error function, which describes its shape. In the sections that follow, we describe a mechanism which provides a means to have such a lateral shearing.

## 3.2 The Hartmann Mask as a lateral shearing interferometer

In 1900, Hartmann proposed a simple method for testing of optical components, that uses a mask of holes periodically arranged on a grid. The holes divide the incoming light into smaller beams which are deflected from the normal according to local tilts in the wavefront (see Fig. [3.2\(a\)](#)).

This section describes the theoretical foundation of the classical Hartmann mask. For simplicity, a 1-dimensional explanation is given.

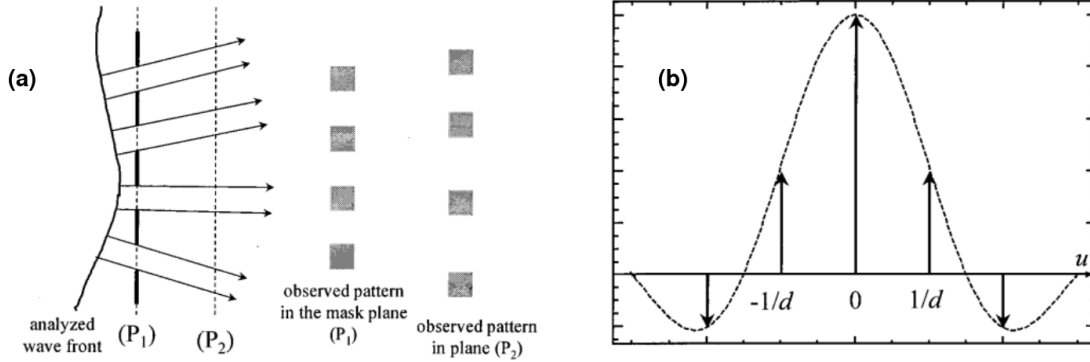


FIGURE 3.2: (a) Principle of the Hartmann mask.  $P_1$  is the plane of the mask,  $P_2$  is a certain distance ahead of it. (b) Diffraction orders in a sinc envelope. Taken from [Primot and Guérineau \(2000\)](#)

Transmittance from periodic array of apertures with pitch ' $d$ ' and size ' $a$ ' can be written as

$$t(x) = \Pi_a(x) * \text{comb}_d(x) \quad (3.2)$$

where  $\Pi_a$  is a rectangular function of width  $a$  ( $=1$  in  $[-a/2, a/2]$  and  $0$  elsewhere) and  $\text{comb}_d(x)$  is a comb of Dirac delta functions spaced  $d$  distance apart.

Amplitudes of the diffraction orders is given by a Fourier transform

$$FT(u) = \frac{\sin \pi u a}{\pi u a} \text{comb}_{1/d}(u) \quad (3.3)$$

The pitch and hole size can be manipulated such that the sinc function in (3.3) decreases fast and only orders  $0$  and  $\pm 1$  are significant, so that the transmittance from the mask can be approximated as a sum of these orders:

$$t(x) = C_o + C_1 \exp(2i\pi x/d) + C_{-1} \exp(-2i\pi x/d) \quad (3.4)$$

where  $C_i$  are the amplitudes of the respective diffraction orders. The zeroth order propagates along the normal of the mask plane. The orders  $\pm 1$  are phase delayed and propagate at angles  $\pm \lambda/d$  with respect to it. At multiples of a certain distance, called the Talbot distance, the phase delay is equal to  $2n\pi$  and the diffracted orders are also laterally shifted (see Fig 3.3).

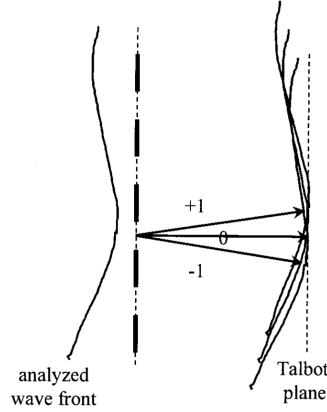


FIGURE 3.3: Hartmann test as a lateral shearing interferometer. The pattern corresponds to three replicas of the incident wavefront that constructively interfere at the Talbot distance. Taken from [Primot and Guérineau \(2000\)](#)

The phase acquired for an optical path length  $g(x)$  is given as  $E_i = \exp(2\pi i g(x)/\lambda)$ . To arrive at the interferogram  $I(x, z)$  at a distance  $z$  from the mask, we first write the scalar electric field by the three orders of an arbitrary wavefront diffracted from the Hartmann mask:

$$E(x, z) = \sum_{p=0, \pm 1} C_p \exp \left[ \frac{2\pi i}{\lambda} (x \sin \theta_p + z \cos \theta_p) + g(x - z \tan \theta_p) \right] \quad (3.5)$$

Where the second term accounts for the shape of the wavefront. Here  $\theta_p = \sin^{-1}(\lambda p/d)$ .  $I(x, z) = EE^*$  and it simplifies to the following:

$$I(x, z) = M_0 + M_1 \cos \left[ \frac{2\pi}{d} \left( x - z \frac{dg}{dx} \right) \right] + M_2 \cos \left[ \frac{4\pi}{d} \left( x - z \frac{dg}{dx} \right) \right] \quad (3.6)$$

where  $M_0 = C_0^2 + 2C_1^2$  ;  $M_1 = 4C_0C_1 \cos(\pi\lambda z/d^2)$  ;  $M_2 = 2C_1^2$

The first term is a constant and of no pertinence in reconstructing the wavefront. The other two terms can be viewed as a frequency modulation of a carrier cosine wave of frequency  $2\pi/d$  with a factor proportional to the product of transverse wavefront slope times a magnification factor of  $z$ . A numerical demodulation will give the derivative of the wavefront error.

Contrast of the second term varies cosinusoidally along  $z$  with a period of  $d^2/\lambda$ . For monochromatic light, this contrast degrades heavily at regular intervals, and the interferogram has to be obtained in the vicinity of Talbot planes. For polychromatic

light, visibility of self-images decreases with  $z$  and the interferogram can only be analyzed in close vicinity of the mask. Due to these shortcomings, the regular Hartmann mask has a limited scope for use.

### 3.3 The Modified Hartmann Mask (MHM)

Primot and Guérineau (2000) suggested a modification to the Hartmann mask to improve its versatility. They proposed complementing the mask with a phase chessboard (see Fig. 3.4). The pitch of this chessboard is twice that of the mask, and it has a depth corresponding to a phase difference of  $\pi$  for a particular wavelength. Thus, alternate square apertures have  $\pi$  phase difference with respect to each other.

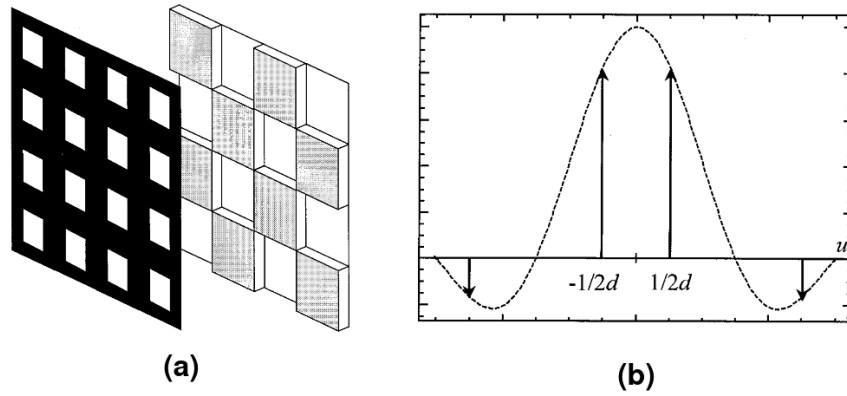


FIGURE 3.4: (a) Hartmann mask with addition of a phase chessboard. (b) Diffraction orders for MHM for  $a = 2d/3$ . The two central orders store the maximum energy. Look at 3.2(b) for comparison. Taken from Primot and Guérineau (2000)

Transmission from this modified Hartmann mask is written as

$$tp(x) = \Pi_a(x) * [\text{comb}_d(x) \exp(i\pi x/d)] \quad (3.7)$$

where the exponential models the alternating phase. The amplitudes of diffracted orders are:

$$FT_p(u) = \frac{\sin(\pi ua)}{\pi ua} [\text{comb}_{1/d}(u) * \delta(u - 1/2d)] \quad (3.8)$$

Which means that the orders have been shifted by  $1/2d$  and there are two prominent diffraction orders at angles  $\pm\lambda/2d$  (see Fig 3.4(b)). The pitch and aperture size are



set such that ( $a = 2d/3$ ) most of the energy is contained in these two orders and the transmission can be approximated as:

$$tp(x) = C_{1/2} \exp(i\pi x/d) + C_{-1/2} \exp(-i\pi x/d) \quad (3.9)$$

Here  $C_{1/2} = C_{-1/2}$  and the interferogram for a general aberrant wavefront comes out as follows:

$$tp(x, z) = 2C_{1/2}^2 \left[ 1 + \cos \left[ \frac{2\pi}{d} \left( x - z \frac{dg}{dx} \right) \right] \right] \quad (3.10)$$

A comparison with 3.6 shows that the **contrast is propagation invariant** (Fig. 3.5) as well as **achromatic**, overcoming the limitations of a regular Hartmann mask. This 1-dimensional explanation shows the use of two diffraction orders interfering to provide a means of lateral shearing. In a 2-dimensional description, this involves 4 orders and the arrangement is called a Quadri-Wave Lateral Shearing interferometer (QWLSI). [Chanteloup (2005) and Velghe et al. (2006)] UPHILL lab uses a wavefront

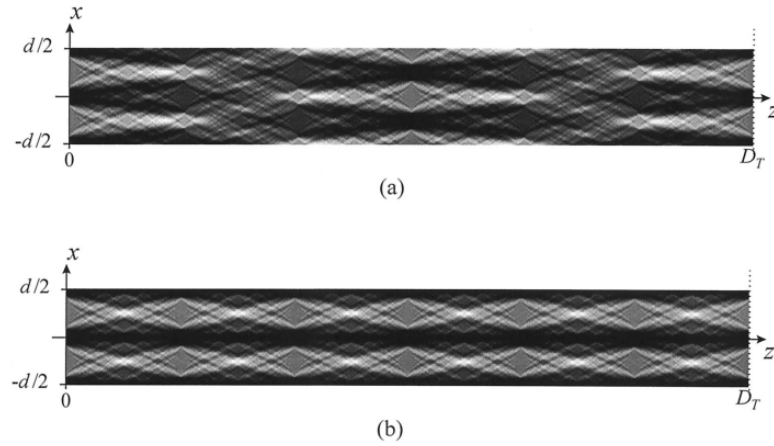


FIGURE 3.5: Numerically calculated intensity for the propagation of the optical field diffracted by the Hartmann mask (a) without and (b) with the phase chessboard, between  $z = 0$  and the first Talbot distance  $D_T$  of the Hartmann mask (in monochromatic illumination). Taken from Primot and Guérineau (2000)

sensor that employs the phase chessboard, with a resolution of 5nm in optical path difference.

## 3.4 The experiments

### 3.4.1 Time evolution of the critical density surface

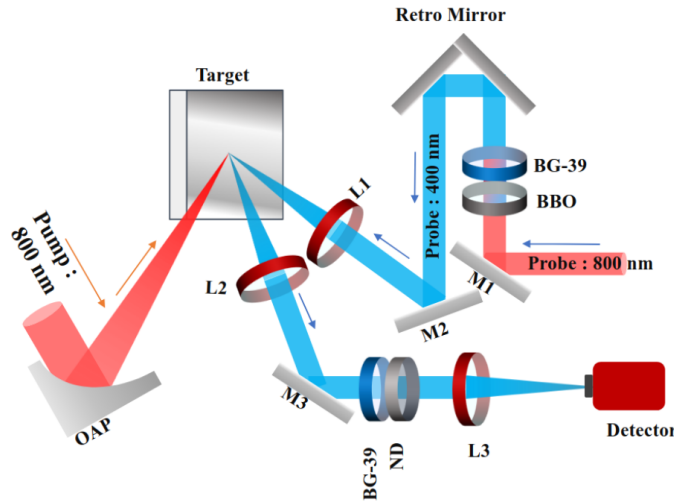


FIGURE 3.6: Experimental setup for pump-probe wavefront measurements.  
(arXiv preprint: [Rakeeb et al. \(2025\)](#))

Fig. 3.6 gives a detailed description of the Pump-Probe setup for wavefront measurements. We use an up-converted 400nm probe for the diagnostics. It is not only easier to align the optics because of its better visibility, but also easier to eliminate any noise coming from the pump's scattered reflection from the plasma surface. This conversion, however, reduces the bandwidth due to phase-matching conditions of the SHG crystal and consequently stretches the pulse in time in addition to its propagation through filters and lenses.

Focal spot of the probe (400 nm) is matched to that of the pump. Surface modulations in critical density surface of plasma created by the pump are captured by reflection of the probe from its irregular surface and routed to the wavefront sensor. BG-39 filters are used to ensure there is no leak of the pump (800 nm) in the probe signal. The signal is also suitably attenuated by neutral density (ND) filters before being fed into the wavefront reconstruction device.

First, the wavefront is recorded by taking reflection of the probe from the smooth metallic surface without the pump. This is done over multiple shots and we take an average to get the reference. At a fixed laser intensity, laser shots are then fired

for each probe delay. Measurements of surface modulations for each delay are then made with respect to the reference.

### 3.4.2 Scaling of surface modulation with intensity

In a much simpler setup, we use only the pump with a dual role-both as the pump and the probe. The pump pulse comes and excites the target. A part of this pulse goes into creating and exciting the plasma. The beam is not entirely absorbed and the reflected part captures modifications introduced by the laser-generated plasma. We measure the wavefront of this reflected pump with the wavefront sensor so as to observe changes in as short a time scale as the pulse width itself.

Before collection into the wavefront sensor, the reflected pump is passed through a filter to exclude extra frequencies coming from the plasma and a neutral density filter to suitably attenuate the signal.

The experiment is run for different laser intensities. Phase plots for each run are analysed using python (see Fig. 3.7). The line-cut for optical path difference is an estimate of the curvature in critical density surface, from which the reflection happens, and is therefore an estimate of the laser ponderomotive force.

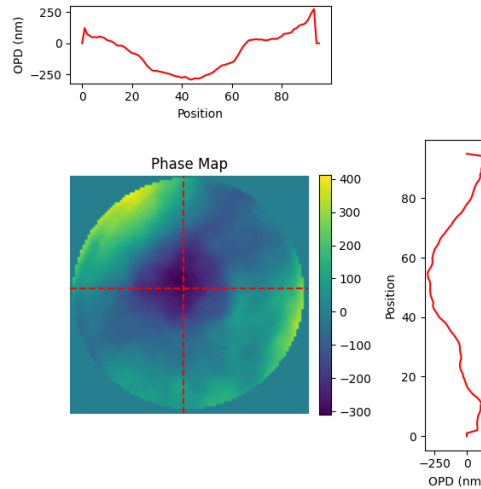


FIGURE 3.7: Result of phase measurement. Phase difference is converted to optical path difference for 800 nm

# Chapter 4

## Results and Conclusions

### 4.1 Time evolution of critical density surface

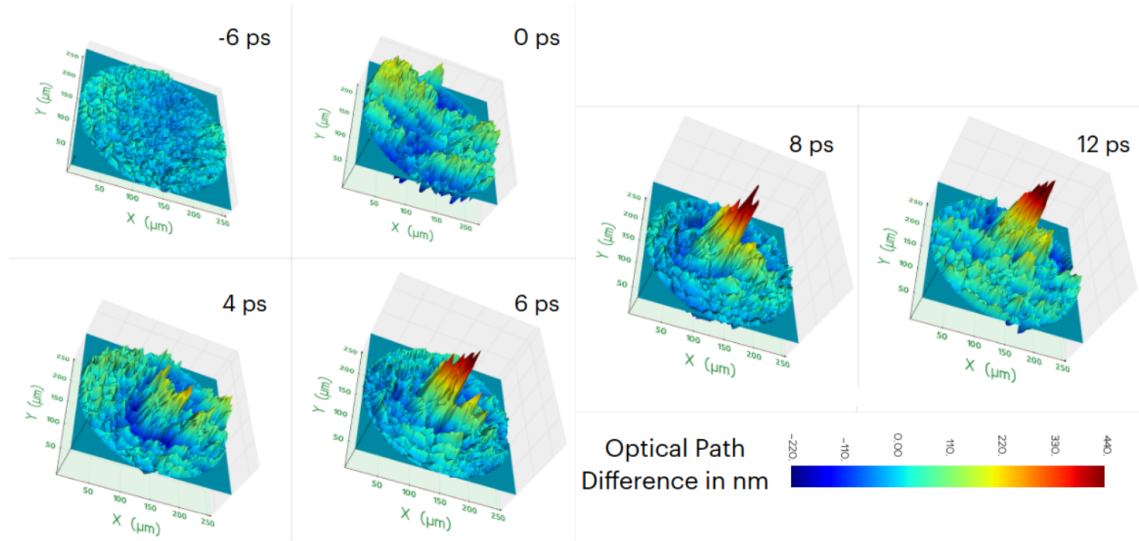


FIGURE 4.1: 3D plot of wavefront measurements for various time delays. arXiv preprint: [Rakeeb et al. \(2025\)](#)

Fig. 4.1 gives a 3D plot of the critical density surface shape for different time delays. For negative delays, there is no dent in the plasma surface as it is reflection from a flat metal surface. At and around  $T_0$ , there is an inward dent in the phase surface showing that the plasma is being pushed inwards by radiation pressure. At positive time delays, the surface shows an outwards expansion of plasma.

These results also prompt us to make some connection with Doppler studies that have been done in the lab under similar experimental conditions.

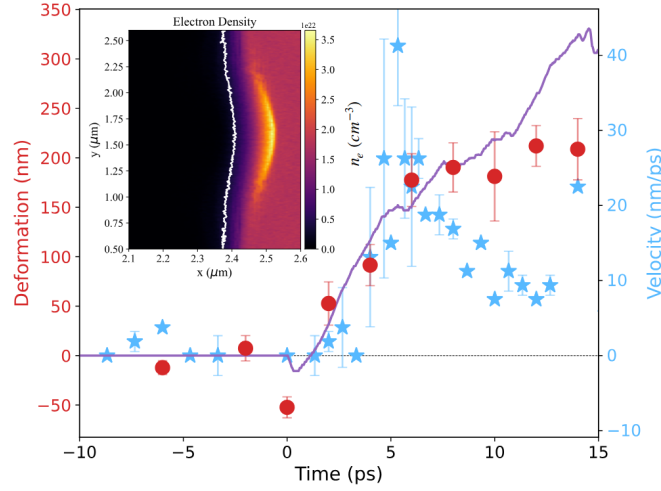


FIGURE 4.2: Surface deformation as a function of delay (Red); Surface velocity from Doppler measurements (Blue Stars, Ref: [Jana et al. \(2018\)](#)); Inset: White line shows the warped critical density in a 2D PIC simulation. arXiv preprint: [Rakeeb et al. \(2025\)](#)

The central pixels of the measured wavefront are averaged, and the corresponding data were plotted alongside Doppler measurements (Fig. 4.2). Plasma velocity sharply increases around 5 ps, coinciding with a rapid rise in the surface deformation. Beyond this, the plasma expansion decelerates, leading to a slower evolution.

## 4.2 Critical surface curvature at different intensities

The experiment is done for different peak intensities and the results are described in the plot that follows. The curvature of critical density surface is radially inwards and reaches as much as half the laser wavelength for the highest intensity ( $a_0 \approx 3.75$ ) used in the experiment. Evidently more curvature is seen for higher intensities.

Interestingly, this inward curvature is only seen in the pump reflection geometry. Pump-Probe measurements at a longer timescale only show a plasma expanding freely outwards, meaning that the phenomenon responsible for the inward curvature has to be as short-lived as the laser pulse width. Since the ponderomotive force

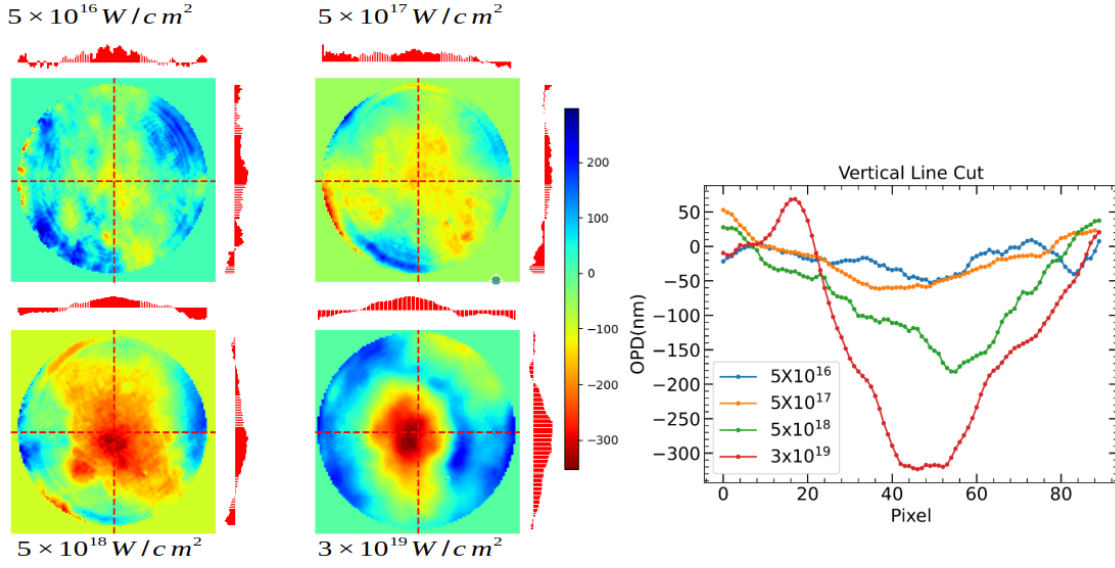


FIGURE 4.3: Phase plots and corresponding line cuts for curvature of critical density surface at different laser intensities (in  $W/cm^2$ ). [Courtesy: Sk Rakeeb]

( $\sim \nabla E^2$ ) lasts only for the pulse duration, the experiment is an optical measurement of this phenomenon, and a first one at that.

There is an ongoing collaboration with a theory and simulation group to look for similarities between what is expected from simulations and what is observed experimentally. A thorough explanation of the results is yet to be made.

### 4.3 Future prospects for wavefront measurement

Various modifications can be made on the pulse which would also serve as a test of our claim. They have been describe below:

1. To shape the intensity/field profile in the transverse direction, a specialized optic known as a [beam homogenizer](#) can be used.
2. Laser absorption mechanisms crucially depend upon the scale length. By using a second harmonic (400nm) conversion crystal whose conversion depends upon  $I^2$ , a pulse with a weaker pre-pulse can be obtained, so that the plasma is only created immediately before the arrival of the femtosecond peak and the pre-plasma scale length is short.

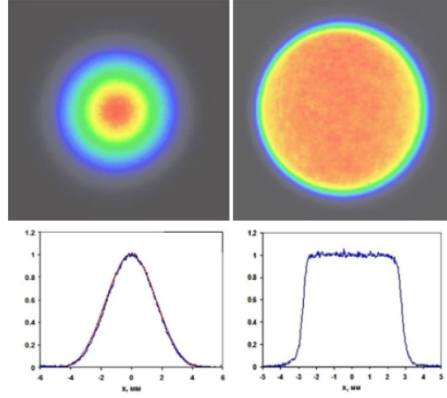


FIGURE 4.4: Shaping of transverse beam profile at focus with a beam homogenizer. Left (Gaussian) and Right (Top-Hat). Taken from [Edmund Optics website](#)

All of these modifications are planned for future experiments at UPHILL, TIFR.

[NOTE:] Images used in this report are either created by me or sourced from the respective authors who have been appropriately cited. Use of images from the experimental results presented in the report without permission of the authors is prohibited.

# References

- Aparajit, C., Jana, K., Lad, A.D., Ved, Y.M., Couairon, A., Kumar, G.R., 2021. Efficient second-harmonic generation of a high-energy, femtosecond laser pulse in a lithium triborate crystal. *Opt. Lett.* 46, 3540–3543. URL: <https://opg.optica.org/ol/abstract.cfm?URI=ol-46-15-3540>, doi:10.1364/OL.423725.
- Asplund, M.C., Johnson, J.A., Patterson, J.E., 2019. The 2018 nobel prize in physics: Optical tweezers and chirped pulse amplification. *Analytical and Bioanalytical Chemistry* 411, 5001–5005. URL: <https://doi.org/10.1007/s00216-019-01913-z>.
- Chanteloup, J.C., 2005. Multiple-wave lateral shearing interferometry for wave-front sensing. *Applied Optics* 44, 1559. URL: <https://opg.optica.org/abstract.cfm?URI=ao-44-9-1559>, doi:10.1364/AO.44.001559.
- Eliezer, S., 2002. *The Interaction of High-Power Lasers with Plasmas*. CRC Press, Boca Raton. doi:10.1201/9781420033380.
- Iaconis, C., Walmsley, I.A., 1998. Spectral phase interferometry for direct electric-field reconstruction of ultrashort optical pulses. *Optics Letters* 23, 792–794. URL: <https://opg.optica.org/ol/abstract.cfm?uri=ol-23-10-792>, doi:10.1364/OL.23.000792. publisher: Optica Publishing Group.
- Jana, K., Blackman, D., Shaikh, M., Lad, A., Sarkar, D., Dey, I., Robinson, A., Pasley, J., Kumar, G.R., 2018. Probing ultrafast dynamics of solid-density plasma generated by high-contrast intense laser pulses. *Physics of Plasmas* 25, 013102. doi:10.1063/1.5005176.
- Kruer, W., 2003. *The Physics of Laser Plasma Interactions*. Frontiers in Physics, CRC Press. URL: <https://www.taylorfrancis.com/books/mono/10>.



- [1201/9781003003243/physics-laser-plasma-interactions-william-kruer](https://doi.org/10.1201/9781003003243/physics-laser-plasma-interactions-william-kruer), doi:[10.1201/9781003003243](https://doi.org/10.1201/9781003003243).
- Kruer, W.L., Estabrook, K., 1985. J×b heating by very intense laser light. The Physics of Fluids 28, 430–432. URL: <https://doi.org/10.1063/1.865171>, doi:[10.1063/1.865171](https://doi.org/10.1063/1.865171).
- Macchi, A., 2013. Electron Acceleration. Springer Netherlands, Dordrecht. pp. 59–79. URL: [https://doi.org/10.1007/978-94-007-6125-4\\_4](https://doi.org/10.1007/978-94-007-6125-4_4), doi:[10.1007/978-94-007-6125-4\\_4](https://doi.org/10.1007/978-94-007-6125-4_4).
- Mulser, P., Bauer, D., 2010. The Ponderomotive Force and Nonresonant Effects. Springer Berlin Heidelberg, Berlin, Heidelberg. pp. 193–227. URL: [https://doi.org/10.1007/978-3-540-46065-7\\_5](https://doi.org/10.1007/978-3-540-46065-7_5), doi:[10.1007/978-3-540-46065-7\\_5](https://doi.org/10.1007/978-3-540-46065-7_5).
- Primot, J., Guérineau, N., 2000. Extended Hartmann test based on the pseudoguiding property of a Hartmann mask completed by a phase chessboard. Applied Optics 39, 5715–5720. URL: <https://opg.optica.org/ao/abstract.cfm?uri=ao-39-31-5715>, doi:[10.1364/AO.39.005715](https://doi.org/10.1364/AO.39.005715). publisher: Optica Publishing Group.
- Rakeeb, S., Dam, S., Parab, A., Lad, A., Ved, Y.M., Kumar, G.R., 2025. Capturing the three dimensional, nano-scale, pico-second dynamics of plasma mirrors with intense ultrashort laser wavefront measurement. URL: <https://arxiv.org/abs/2505.02403>, arXiv:[2505.02403](https://arxiv.org/abs/2505.02403).
- Siegman, A.E., 1986. Lasers. University Science Books.
- Strickland, D., Mourou, G., 1985. Compression of amplified chirped optical pulses. Optics Communications 56, 219–221. URL: <https://www.sciencedirect.com/science/article/pii/0030401885901208>, doi:[https://doi.org/10.1016/0030-4018\(85\)90120-8](https://doi.org/10.1016/0030-4018(85)90120-8).
- Strojnink, M., Paez, G., Mantravadi, M., 2007. Lateral Shear Interferometers. John Wiley Sons, Ltd. chapter 4. pp. 122–184. URL: <https://onlinelibrary.wiley.com/doi/abs/10.1002/9780470135976.ch4>, doi:<https://doi.org/10.1002/9780470135976.ch4>.

- Velghe, S., Primot, J., Guerineau, N., Ha"idaya, R., Demoustierb, S., Cohenc, M., Wattellier, B., 2006. Advanced wave-front sensing by quadri-wave lateral shearing interferometry - art. no. 62920e, pp. 62920E–1. doi:[10.1117/12.681533](https://doi.org/10.1117/12.681533).
- Weiner, A.M., 2009. Ultrafast-Pulse Measurement Methods. John Wiley Sons, Ltd. chapter 3. pp. 85–146. URL: <https://onlinelibrary.wiley.com/doi/abs/10.1002/9780470473467.ch3>.